Biosensors and Bioelectronics 119 (2018) 10–17

Contents lists available at ScienceDirect

Biosensors and Bioelectronics

journal homepage: www.elsevier.com/locate/bios

Au nanoparticles functionalized 3D-MoS_2 nanoflower: An efficient SERS matrix for biomolecule sensing

Shib Shankar Singha[a,b], Suchanda Mondal[c], Tara Shankar Bhattacharya[a], Laboni Das[d], Kamalika Sen[d], Biswarup Satpati[c], Kaustuv Das[e], Achintya Singha[a,*]

[a] Department of Physics, Bose Institute, 93/1, Acharya Prafulla Chandra Road, Kolkata 700009, India
[b] Department of Physics, Brahmananda Keshab Chandra College, 111/2 B. T. Road, Bonhooghly, Kolkata 700108, India
[c] Saha Institute of Nuclear Physics, 1/AF Bidhannagar, Kolkata 700064, India
[d] Department of Chemistry, University of Calcutta, 92, APC Road, Kolkata 700009, India
[e] Department of Physics, Jadavpur University, Kolkata 700032, India

ARTICLE INFO

Keywords:
MoS_2 nanoflower
Gold functionalized MoS_2 nanoflower
Optical property
Surface Enhanced Raman Scattering (SERS)
Biosensor
Bilirubin sensing

ABSTRACT

Fabrication of Molybdenum disulfide (MoS_2) nanostructures and surface functionalization with noble metal nano particles is an emerging field of research as it has potential applications in electronic devices and chemical sensing. Here we report application of gold nanoparticles (AuNPs) decorated MoS_2 nanoflowers (Au-MoS_2 NFs) as an efficient bio-sensor. MoS_2 NFs, synthesized using green synthesis process, are further functionalized with AuNPs to tune their physical properties and make them more appropriate for biological applications. The abundant '*hot-spots*' created by AuNPs through localization of electromagnetic field endows the Au-MoS_2 hybrid structure as an excellent substrate for biochemical sensing through surface enhanced Raman scattering (SERS). The sensing efficiency of the SERS substrate is examined using Rh6G as probe molecule with concentration as low as 10^{-12} M. Main emphasis is given in detecting free bilirubin, an important component of human blood, using SERS technique. Au-MoS_2 NF SERS substrate exhibits high sensitivity, stability and excellent reproducibility in sensing bilirubin from high level (10^{-3} M) to picomolar level. The concentration (C) dependent SERS intensity (I) is found to follow the general relationship $I = C^{\alpha}$, with α ranging from 0.09 to 0.12. The substrate shows excellent selectivity and reliability while sensing of free bilirubin performed in human serum in the presence of crucial interferences such as dextrose, cholesterol and phosphate. In the present study, this Au-MoS_2 hybrid offers a new potential biosensing technology for free bilirubin detection and is anticipated to be applied for clinic diagnosis.

1. Introduction

During the past few years, intensive research interest has been growing in the study of transition metal di-chalcogenides (TMDs) such as MoS_2, $MoSe_2$, WS_2, etc. owing to their unique optical properties and potential applications in nanotechnologies, biosensor, etc. (Gan et al., 2017; Lauritsen et al., 2007; Lee et al., 2013; Rao and Govindaraj, 2009; Tenne, 2006;). A number of techniques have been used like micro-mechanical exfoliation, chemical exfoliation, electrochemical, and lithium intercalation for the preparation of TMD sheet in atomic level (Chou et al., 2013; Coleman et al., 2011; Das et al., 2016; Eda et al., 2011; Radisavljevic et al., 2011; Zeng et al., 2011). But these methods have some limitations to control the size, shape and dimension and to produce a large amount of material (Radisavljevic et al., 2011). Presently, there is a trend towards the fabrication of nanostructures, like fullerene, nano sphere, onion like carbon nano particles, due to their high surface to volume ratio. These 3-dimensional (3D) structures enhance the surface effect that increases the efficiency for applications in optical detection, chemical and biosensing etc. To prepare MoS_2 nanostructure, various methods have been used like hydrothermal, gas phase reaction, sonochemical synthesis, laser ablation, thermal decomposition, magnetron sputtering, electron-beam and microwave irradiation techniques (Chhowalla and Amaratunga, 2000; Feldman et al., 1995; Mdleleni et al., 1998; Veeramalai et al., 2015; Vollath and Szabó, 1998; Wang et al., 2015; Xu et al., 2014; Zelenski and Dorhout, 1998). Among them, hydrothermal synthesis is a good choice as it doesn't require toxic and hazardous gases and high process temperature and overall provides good control over the morphology of the structures

* Corresponding author.
E-mail address: achintya@jcbose.ac.in (A. Singha).

https://doi.org/10.1016/j.bios.2018.07.061
Received 11 May 2018; Received in revised form 13 July 2018; Accepted 28 July 2018
Available online 30 July 2018

(Ma et al., 2008; Tang et al., 2013).

Control on sulphur ratio in MoS_2 is important because the polarity and optical property of the material depends on the vacancy and abundance of sulphur atoms (McDonnell et al., 2014). It is reported that sulphur-rich MoS_2 nanostructures finds the applications in electrochemistry, catalyst and electronic devices due to the availability of active surface states (Krishnamoorthy et al., 2014; McDonnell et al., 2014; Xie et al., 2013). However, only designing of the nanostructure is not sufficient for applications such as detection and sensing of organic and biomolecules due to their weak interaction with MoS_2 (Ling et al., 2014). A considerable amount of efforts have been employed for functionalization of MoS_2 surface with different noble metal nano particles (MNPs) to improve the intrinsic (and/or reactive) property of the material (Huang et al., 2013; Shi et al., 2013; Singha et al., 2017; Sreeprasad et al., 2013; Su et al., 2014; Yuwen et al., 2014). However, functionalization methods require certain reducing and stabilizing agents such as thiol, trisodium citrate (Huang et al., 2013), hydroxyl amine (Sreeprasad et al., 2013) carboxymethyl cellulose (Su et al., 2014) and ascorbic acid (Yuwen et al., 2014). But a simpler and reliable method with less number of reagents for functionalization of MoS_2 with MNPs is more acceptable for applications.

Sensing of organic and bio-molecules, having toxicologically important roles in life processes, is becoming an essential perspective of medical and environmental sciences. Bilirubin is a vital biomolecule as its presence above 50 μM can cause liver problems like hepatitis and liver-cirrhosis etc. Increased levels of bilirubin in infants can cause brain haemorrhage. On the other hand bilirubin also exhibits potent antioxidant and anti-inflammatory properties (Baranano et al., 2002). Low bilirubin level in blood is also known to cause certain complications like diabetic nephropathy, diabetic retinopathy, cardiovascular diseases and chronic kidney diseases (Fukui et al., 2008; Sekioka et al., 2015; Tanaka et al., 2014). Extensive attempts have therefore been made to develop new and effective free bilirubin sensors for clinical diagnostics in recent years (Rahman et al., 2008; Santhosh et al., 2014; Shoham et al., 1995). A variety of redox-enzymes and enzyme-electrode was applied for the amperometric determination of bilirubin (Rahman et al., 2008; Shoham et al., 1995). But the use of enzyme makes the method expensive and lowers the stability (Rahman et al., 2008). The quenching of fluorescence intensity of Human Serum Albumin (HSA)-AuNCs with the increase of bilirubin concentration has been reported as the method for the detection of free bilirubin (Santhosh et al., 2014). The D-glucuronic acid and pentadecylphenol polyfluorene conjugated with HSA are used for bilirubin detection by fluorescent technique (Senthilkumar and Asha, 2013, 2015). Raman spectroscopy is a non-destructive tool for molecular detection as it provides the fingerprint of the molecule. The limitation of detection at low molecular concentration using Raman technique due to its weak scattering process can be overcome by Surface enhanced Raman Spectroscopy (SERS). This technique enhances Raman signal of the molecules by a factor of 10^{13}–10^{15} when adsorbed on rough metal surfaces due to electromagnetic and chemical enhancements and provide a fingerprint of a molecule at ultralow concentration level (An et al., 2012; Emory et al., 1998; Junga et al., 2013; Lee et al., 2011; Majumdar et al., 2013; Wei et al., 2013;). Nanostructures decorated with MNPs act as a stable and efficient substrate for SERS amplification. In the gap between metal nano particles, an enormous enhancement of electromagnetic field takes place (known as *hot spots*) due to the plasmon coupling effect that allows us to detect single molecule adsorbed at the *hot spot* (Li et al., 2017; Emory et al., 1998; Graham et al., 2008; Jiang et al., 2017; Lin et al., 2013; Majumdar et al., 2013; Qian and Nie, 2008; Yigit et al., 2011). Sulk et al. (1999) have reported the detection of bilirubin at micro molar concentration using Ag colloid through SERS measurements. As both high and low bilirubin level in blood is harmful, an assay which can determine both the levels is highly desirable. Recently, Liang et al. (2018) have demonstrated the use of gold nanoparticles (AuNPs) decorated three-dimensional MoS_2 nanospheres as SERS sensor for the detection of melamine in milk. Stable metal clusters with narrow interior gaps and the large surface area are required to enhance the SERS response of a substrate which allows detecting molecules at ultra low concentration.

In this report, MoS_2 nanoflower (MoS_2 NFs) are synthesized by hydrothermal technique and are found to be enriched with more active sites due to abundant unsaturated sulphur which provides an opportunity for functionalization with MNPs. Au NPs are uniformly grown throughout the MoS_2 NFs surface without using a reducing agent. The optical and electronic properties of the MoS_2 NFs and AuNPs decorated MoS_2 NFs (Au-MoS_2 NFs) have been studied using Raman and photoluminescence spectroscopy. The main aim of this report is to use the Au decorated MoS_2 NFs as an efficient substrate for biomolecule sensing using SERS technique. Due to the presence of the petals, the MoS_2 NFs provides high surface area to adsorb molecules compared to MoS_2 nanosphere. To check the SERS efficiency of the Au-MoS_2 NF hybrid, an aromatic dye molecule (Rh6G) was detected up to 10^{-12} M concentration. Finally, the substrate was used for bilirubin sensing down to 10^{-7} M in human serum (HS) matrix. It is found that the as-fabricated substrate is highly efficient to detect the bilirubin below normal level (< 25 μm/L) to danger level (> 50 μm/L). The Au-MoS_2 substrate exhibits a high degree of selectivity towards bilirubin in human serum even in the presence of dextrose, cholesterol and phosphate. Here, we suggest Au-MoS_2 NF hybrid as a low-cost substrate that utilizes the combination of MoS_2 NF and Au NPs for high-performance sensing of biomolecule beyond the medical diagnosis.

2. Materials and methods

2.1. Chemical used

Molybdic oxide (MoO_3) as source of Mo, Potassium thiocyanate (KSCN) for sulphur reagent and SDS as a surfactant with 99.98% purity were purchased from MERCK, India. $HAuCl_4{\cdot}3H_2O$, Rh6G and free bilirubin were bought from Sigma Aldrich. Millipore water was used for the entire synthesis process. Assayed chemistry control human serum (HS) was obtained from Lypochek (Bio-Rad laboratories, Irvine CA, containing $\sim 2 \times 10^{-5}$ M total bilirubin as per the assay kit). Cholesterol was obtained from LOBA Chemie, disodium hydrogen phosphate dihydrate and anhydrous dextrose was obtained from Merck (India). All the chemicals were used as received and used without further purification.

2.2. Preparation of MoS_2 NFs

In a typical synthesis, 30 mmol MoO_3 (about 4.31 gm) and 75 mmol KSCN (about 7.20 gm) and SDS (0.20 gm) were mixed in a 90 ml distilled water. The molar ratio of MoO_3 and KSCN was maintained at 1:2.5 to get a sulphur-rich sample. Then this solution was vigorously stirred for 1 h to make a homogenous mixture. The final solution was transferred into a 120 ml capacity Teflon lined stainless still autoclave and heated at 180 °C for 24 h. After cooled down to room temperature, the resultant precipitate was washed ten times with distilled water by centrifugation. Finally, the MoS_2 powder was obtained after heating the washed sample in a tube furnace at 80 °C for 6 h under nitrogen gas flow.

2.3. Synthesis of Au NPs on MoS_2 NFs

MoS_2 NFs decoration with Au NPs was performed in three neck flux by hydrothermal method. In this process, 2.4 mM $HAuCl_4$ solution was boiling inside flux and then 50 mg MoS_2 NFs was added and heated for an additional 3 min under vigorous stirring (Polyakov et al., 2014). The mixture was then stirred for 30 min and cooled down to room temperature. The molar ratio of $HAuCl_4/MoS_2$ was maintained at 2.4:1. High purity Ar gas was flown during the whole process to avoid the

oxidization during the reaction. The Au NP decorated MoS_2 sample was used for the detection of the molecule using SERS technique after washing. The SERS sample preparation method is described in Supplementary Note 1.

2.4. Instrument used for sample characterization

Powder X-ray diffraction (XRD) pattern was recorded using a Rigaku (MiniFlex II) diffraction system with high-intensity CuKα radiation. Surface morphology was studied by Field emission scanning electron microscopy (FESEM, INSPECT F50) operated at an accelerating voltage of 5.0 kV. Optical absorption spectroscopy was carried out by Lambda-25 (Perkin Elmer). TEM analysis was performed in FEI, TECNAI G2 F30. Raman and PL measurements were carried out using a micro Raman Spectrometer (LabRam HR, Jobin Yvon) equipped with Peltier cooled CCD detector at room temperature. Argon ion laser (488 nm) and He-Ne laser (633 nm) were used as excitation sources, and 50X objective was used to focus the laser beam on the sample. The laser power for 488 nm (633 nm) was 200 μW (100 μW) and the acquisition time was 10 s for both the lasers.

3. Results and discussion

The schematic representation of the sample preparation using hydrothermal method is presented in Fig. 1A. The field-emission scanning electron microscopy (FESEM) image displayed in Fig. 1B reveals the flower-like morphology of the MoS_2 which are spherical with a mean diameter of 1.5 μm. Several MoS_2 flakes, with an average thickness of 6 nm, form the nanopetals of the nanoflowers as appeared in the magnified image (Fig. S1A). Transmission electron microscope (TEM) image (Fig. 1C) confirms the layer structure of MoS_2. High-resolution TEM images (see Fig. S1 B,C) show "surface ripples" due to flexible and weak van der Waals (vdW) adhesion of the atomic layers (Kushim et al., 2015). Therefore, the edges of the MoS_2 2D layers bend easily and finally form flower-like structure as shown schematically in Fig. 1A. The cleaved lattice structures, the relative orientation of planes and atomic dislocations observed in HRTEM images prove that the MoS_2 NFs are defect-rich (Wang et al., 2014; Xie et al., 2013).

The phase and the crystal structure were analyzed by XRD measurement shown in Fig. 1D. The XRD peaks at angles 12.40°, 32.67°, 38.45°, 58.42° correspond to the (002), (100), (103), and (110) planes of hexagonal phase of MoS_2 (2H-MoS_2) (Ramadoss et al., 2014; Wu et al., 2015). The selected area electron diffraction pattern of MoS_2 NF (Fig. S2) also confirms their hexagonal structure. The broadening of the (103) and (110) peaks and shift of (002) peak are consistent with the formation of defect-rich nanosized flowers (Wu et al., 2015) as observed in TEM analysis.

The Raman spectrum of the sample is shown in Fig. 1E. As the measurement was performed at low laser power we assume that there is no laser induced heating during measurements. The observed Raman modes are fitted with Lorentzian functions. Raman bands at 381 cm^{-1} and 405.4 cm^{-1} are for the E^1_{2g} (in plane) and A_{1g} (out of plane) vibrational modes of 2H-MoS_2, respectively. The vibrational patterns are shown in the inset of Fig. 1E. The gap of 24.4 cm^{-1} between the two modes indicates that the 2D flakes which form the nanopetals of MoS_2 NF are few-layered (~ 4 layers) (Lee et al., 2010). It is observed that E^1_{2g} mode has a larger peak width and low intensity compared to the A_{1g} mode, which suggests the existence of disorders or defects in the basal plane direction (Kong et al., 2013; Wu et al., 2015). Moreover, low intensity of E^1_{2g} modes reveals that basal plane of MoS_2 NF is sulphur rich (Kong et al., 2013; Yan et al., 2013). The sulphur-rich MoS_2 has been reported as a p-type material (McDonnell et al., 2014).

Photoluminescence (PL) measurement was carried out to study the electronic property of the material. Fig. 1F shows the PL spectrum of the MoS_2 NFs. The spectrum was deconvoluted with Gaussian functions confirms the existence of three peaks. The two peaks at 600 nm and 642 nm are due to the neutral exciton transitions (A and B excitons) of MoS_2, originating from spin-orbital coupling in valance band at *K* point (Splendiani et al., 2010). The third peak at wavelength 675 nm arises due to the transition of the charged exciton (Buscema et al., 2014; Mouri et al., 2013; Splendiani et al., 2010). Whether the as prepared MoS_2 NF is p-type or n-type can be estimated from the parameter: $\gamma = I_X^-/(I_X^0 + I_X^-)$, where, I_X^0 and I_X^- are the emission intensities of neutral exciton and charged exciton (Buscema et al., 2014; Mouri et al., 2013; Singha et al., 2015). The calculated value of γ is found to be 0.30, (which is lower than sulphur vacant or n-type) signifies the MoS_2 NF to

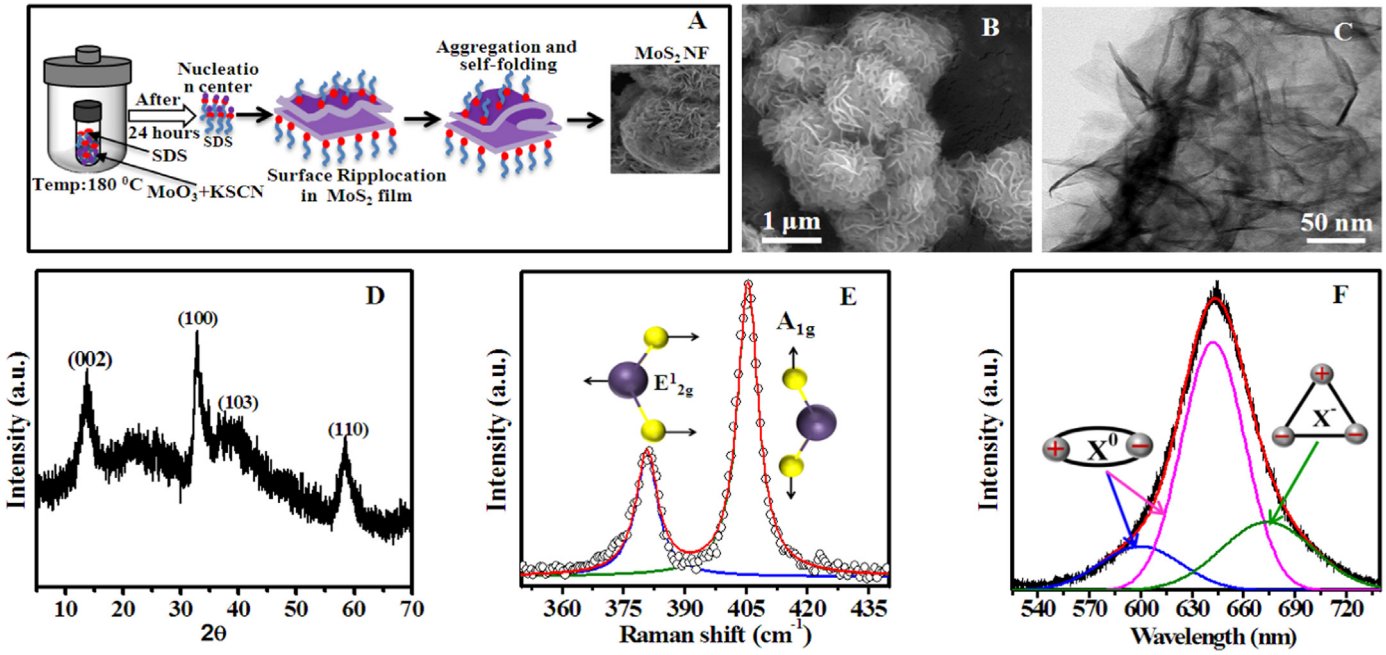

Fig. 1. (A) Schematic presentation of MoS_2 NFs preparation using hydrothermal method. (B) FESEM image and (C) TEM image of MoS_2 NFs. (D) XRD spectrum, (E) Raman spectrum (inset shows the schematic representation of vibrational patterns), and (F) PL spectrum (inset shows the schematic representation of trion and exciton corresponding to the emissions) of MoS_2 NFs.

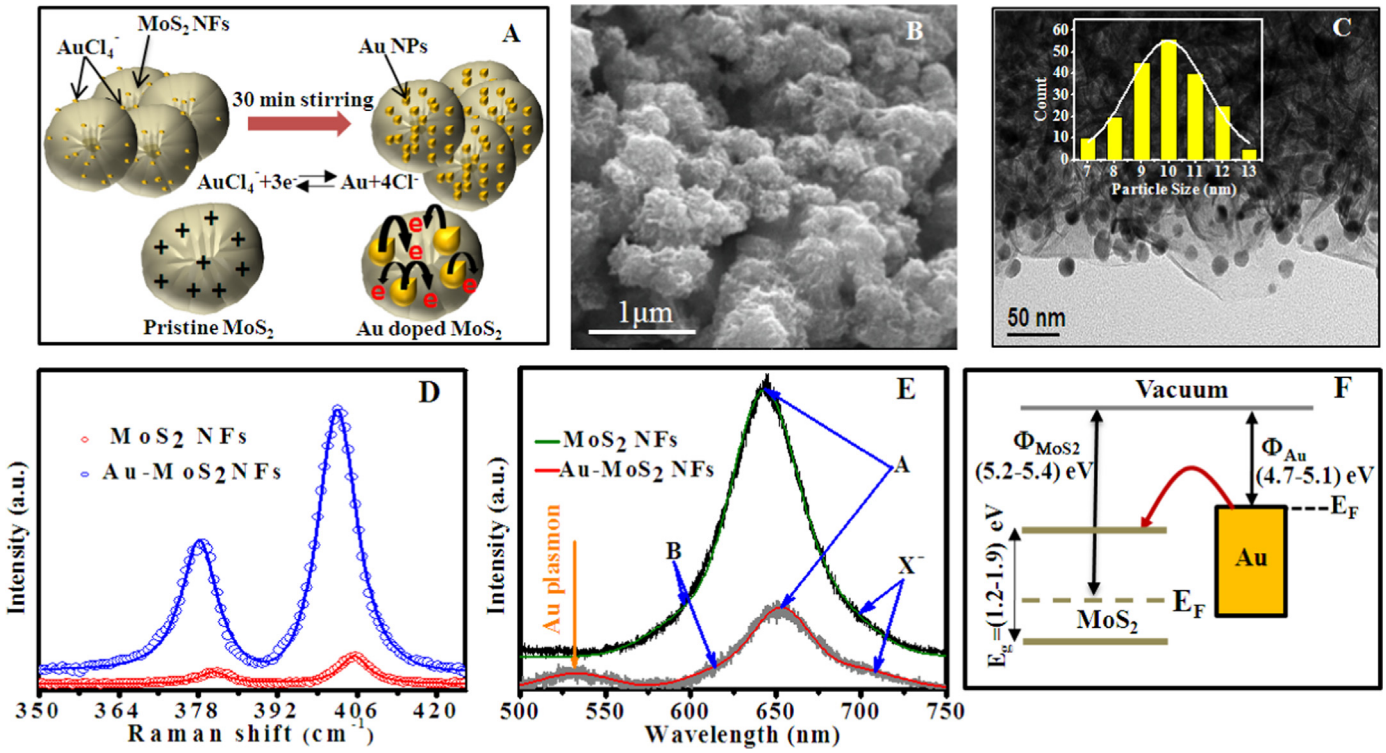

Fig. 2. (A) Schematic representation of the mechanism of Au NPs formation on MoS_2 NFs. (B) SEM image and (C) TEM image of Au-MoS_2 NFs. Inset of (C) shows the histogram of size of Au NPs. (D) Raman spectra of MoS_2 NFs (red circle) and Au-MoS_2 NFs (blue circle). The experimental data are fitted with two Lorentzian functions (red and blue solid lines). (E) PL spectra of MoS_2 NFs (black line) and Au-MoS_2 NFs (grey line). The green and red lines are fitted curves with Gaussian function. (F) The schematic energy band diagram for MoS_2 and Au. The figure shows the relative positions of Fermi level with respect to vacuum level before establishing a contact (Cho et al., 2017). (For interpretation of the references to colour in this figure legend, the reader is referred to the web version of this article.)

be p-type (Buscema et al., 2014; Mouri et al., 2013; Singha et al., 2015). Thus, both Raman and PL studies imply that the MoS_2 NFs are p-type (sulphur rich).

Fig. 2A shows the schematic representation of growth mechanism of AuNPs on MoS_2 NFs surface. The $HAuCl_4$ in water decomposes into $AuCl_4^-$ which is attracted by unsaturated sulphur on the surface of the MoS_2 NFs and acts as a nucleation centre for the formation of AuNP (Xie et al., 2013). Due to the potential difference of $AuCl_4^-$ and MoS_2 (Cho et al., 2017), charge transfer takes place between them and finally Au NPs are formed on the surface of the MoS_2 NFs. The AuNPs were attached on the MoS_2 NF surface by Au-S strong interactions. A uniform and dense $AuNP_S$ were grown throughout the MoS_2 surface as shown in SEM image (Fig. 2 B). The TEM image presented in Fig. 2C and Fig. S3A indicates that the Au NPs are well dispersed on the surface of MoS_2 NFs. The estimated average size of AuNPs is found to be 10 ± 2 nm as shown in the inset of Fig. 2C. Fig. S3B displays HRTEM image where AuNP is attached to the surface ripple of MoS_2. Fig. S3C is the high angle annular dark-field scanning TEM (STEM-HAADF) image of Au-MoS_2 NF and corresponding chemical maps using energy dispersive X-ray spectroscopy of the representative elements showing uniform decoration of MoS_2 NF with Au. Fig. S4 shows the EDX spectra of the MoS_2 and Au-MoS_2 NF. The narrow inter-particle gap makes the Au-MoS_2 NF hybrid suitable as a SERS substrate. UV–visible spectra of $HAuCl_4$, MoS_2 NF and Au-MoS_2 NF are shown in Fig. S5A–C, respectively. The absorption peaks at 590 and 632 nm are observed for MoS_2 NF due to transition from k_4-k_5 and k_1-k_5 in the direct bandgap at k-point brilliune zone (Polyakov et al., 2014). We have also observed another absorption peak at low energy (~ 674 nm) due to the charge exciton. Gold precursor shows strong absorption band at 300 nm which completely diminishes after reaction with MoS_2 NF suggesting that $HAuCl_4$ converts into Au^0 NPs via charge transformation. After complete reaction surface plasmon peak of Au NPs emerges at 530 nm along with MoS_2 peak.

Fig. 2D displays the Raman spectra of pristine and Au decorated MoS_2 NFs. After Au incorporation, the softening and broadening of the A_{1g} and E^1_{2g} phonon modes are observed with respect to the bare MoS_2 NFs. The redshift of both the A_{1g} and E^1_{2g} suggests that the Au NPs acts as n-type dopant and the result is consistent with earlier reports (Chakraborty et al., 2012; Cho et al., 2017; Das et al., 2008). The increase of the Raman mode intensity after Au decoration is due to the enhanced localized electromagnetic field in the vicinity of the AuNPs. The PL spectra of bare and Au decorated MoS_2 NF are presented in Fig. 2E. After AuNPs attachment, the PL intensity of the MoS_2 NF decreases and the emission energies shift towards higher wavelength. A new peak at around 530 nm is observed along with MoS_2 peak which is well-known surface plasmon peak of Au NPs (Cho et al., 2017; Polyakov et al., 2014). The work function of sulphur-rich MoS_2 ranges from 5.2 to 5.4 eV (Cho et al., 2017; McDonnell et al., 2014) whereas the Au has 4.7–5.1 eV (Cho et al., 2017). So on contact electrons are transferred from AuNPs to MoS_2 as shown in Fig. 2F and increases the negative charge carrier concentration of MoS_2 surface. Thus, the AuNPs act as n-type dopant and hence reduce the overall intensity of the PL emission of the MoS_2 NF (Mouri et al., 2013). Due to the charge accumulation on the MoS_2 surface, the Fermi level is realigned at Au-MoS_2 interfaces which results in the redshift of exciton emission (Gong et al., 2014).

3.1. Study of SERS efficiency of MoS_2 NFs with and without Au NPs

To check the sensing ability, the Au-MoS_2 NFs were used as a SERS substrate for the detection of an aromatic molecule (Rh6G). The probe molecule was adsorbed on the surface of the hybrid structure by dipping it into the solutions of the said molecule with various concentrations (1×10^{-4} to 1×10^{-12} M). The measurements were performed with 488 nm laser as excitation sources. To compare the capability of both bare MoS_2 NFs and Au-MoS_2 NFs as SERS substrate, detection of

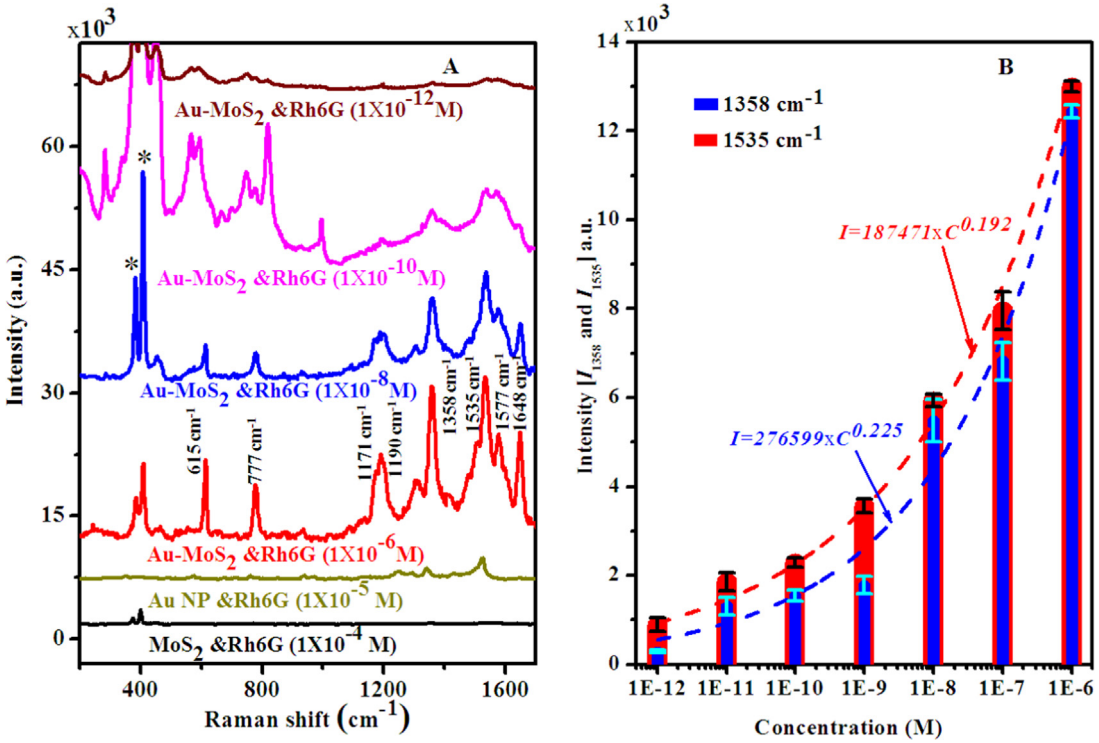

Fig. 3. (A) SERS spectra of Rh6G with concentration ranging from 1×10^{-4} M to 1×10^{-12} M using MoS_2 (black curve), AuNP (dark yellow) and Au-MoS_2 substrate. Asterisk (*)-marked peaks are from the MoS_2. (B) Bar diagram depicting concentration vs intensity plot of 1358 cm^{-1} (I_{1358}, blue bar) and 1535 cm^{-1} (I_{1535}, red bar) modes of Rh6G. The blue and red dash lines are fitted curves according to the power law for modes 1358 cm^{-1} and 1535 cm^{-1}, respectively. Considering all concentration, the average relative standard deviation (RSD) for modes at 1358 cm^{-1} and 1535 cm^{-1} are 7% and 8%, respectively. (For interpretation of the references to colour in this figure legend, the reader is referred to the web version of this article.)

Rh6G was performed for both the substrates. Fig. 3A shows the selective SERS spectra of Rh6G with concentration ranging from 1×10^{-4} to 1×10^{-12} M using bare MoS_2 NFs (black curves), Au NPs (dark yellow), and Au-MoS_2 NFs (all other curves). The SERS spectrum of 1×10^{-4} M Rh6G using bare MoS_2 substrate does not shows any vibration mode. In AuNPs we see an enhancement in Raman signal while a huge enhancement has been observed in Au-MoS_2 hybrid and we can identify the Raman modes of Rh6G clearly up to picomolar concentration. The observed vibrational bands at 615, 777, 1171, 1190,1358, 1535, 1577 and 1648 cm^{-1} are well matched with the previously reported works (Singha et al., 2015; Su et al., 2014). The assignment of the observed Raman modes is presented in Supplementary Note 2. The Rh6G adsorbed on to the hybrid structure via π-π interaction with MoS_2 (Lu et al., 2015). Two well known mechanisms for Raman signal enrichment in SERS are the chemical and electromagnetic enhancement. The chemical enhancement takes place due to charge transfer between the surface of MoS_2 and Rh6G molecule through π-π bond (Lu et al., 2015). Electromagnetic enhancement, which has the major role of the Raman signal enhancement, occurs due to the strong localized electromagnetic field at the interior of AuNPs (Jiang et al., 2017). The sensitivity and the detection limit evaluate the quality of a SERS substrate. To get a quantitative idea about the sensitivity of the Au-MoS_2 SERS sensor we have studied the concentration dependent mode intensity. We considered two strong peaks of Rh6G at 1358 cm^{-1} and 1535 cm^{-1} and estimated their intensities (I_{1358} and I_{1535}) by fitting with Lorentzian functions. At each concentration (C) we have taken the average intensity of at least 5 spectra. Fig. 3B shows the concentration-dependent I_{1358} and I_{1535}. The intensity of both the modes versus C follow the power law relationship ($I_{1358} = 276{,}599 \times C^{0.225}$ and $I_{1535} = 187{,}471 \times C^{0.192}$). The R^2 value (0.98) for both the cases represents the goodness of the fitting. At high concentration of Rh6G, as most of the plasmonic surface is covered up by the molecules, so the rate of increase of SERS peak intensity with increase in Rh6G concentration is low compared to that at low concentration of Rh6G.

To verify the efficiency of the Au-MoS_2 substrate for the biosensing application, SERS study was conducted with the substrate for the detection of free bilirubin in water with concentration ranging from 1×10^{-3} to 1×10^{-12} M using 633 nm laser as excitation source. Fig. 4A shows some selective SERS spectra of bilirubin within the concentration range. However, no vibrational mode of bilirubin was observed when SERS spectrum was measured using MoS_2 NF substrate (black curve). But, in contrast, Au-MoS_2 NF matrix shows excellent potentiality to detect SERS spectrum of the free bilirubin up to pico molar concentration. This is due to the strong affinity of bilirubin towards Au (Maity at al, 2014). The Raman modes appear at 687, 737, 884, 935, 984, 1186, 1264, 1290, 1335, 1346, 1444, 1499, 1561 and 1610 cm^{-1}. The measured modes match well with the previously reported Raman data of bilirubin (He et al., 1995; Sulk et al., 1999). The assignment of the observed Raman modes of Bilirubin is given in Supplementary Note 3.

To get a quantitative idea of signal enhancement, the enhancement factor (EF) has been calculated using the following formula (Majumdar et al., 2013):

$$EF = (I_{SERS}/N_{SERS})/(I_{Ref}/N_{Ref})$$

where, I_{Ref} (I_{SERS}) and N_{Ref} (N_{SERS}) are the intensity of the normal Raman mode (SERS) and the number of molecules in the reference sample (SERS sample), respectively. The estimated value of EF for the bilirubin peak at 1610 cm^{-1} is found to be $\sim 10^9$ which is 2 orders higher than the reported result for the detection of melamine in milk using MoS_2 nanosphere (Liang et al., 2018). The reason behind the higher enhancement factor is that the Au-MoS_2 is the higher surface area for adsorbing probe molecule due to the presence of petals than the AuNP decorated MoS_2 nanosphere. Concentration-dependent average intensity of 5 measurements of the peaks at 1444 cm^{-1} (I_{1444}) and 1610 cm^{-1} (I_{1610}) are given in Fig. 4B. Interestingly, similar to Rh6G,

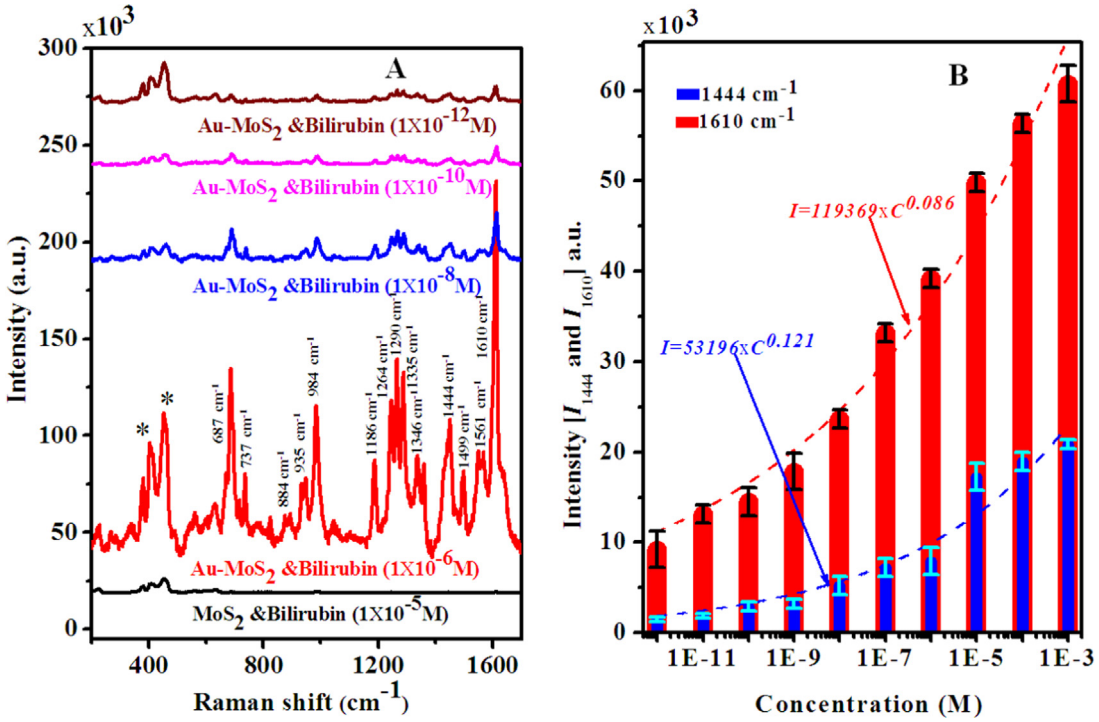

Fig. 4. (A) SERS spectra of bilirubin with concentration ranging from 1×10^{-5} M to 1×10^{-12} M using MoS_2 (black curve) and Au-MoS_2 substrates. Asterisk (*)-marked peaks are from the MoS_2. (B) Bar diagram depicting the concentration vs intensity plot of 1444 cm^{-1} (I_{1444},blue bar) and 1610 cm^{-1} (I_{1610}, red bar) modes of bilirubin. The blue and red dash lines are fitted curves according to the power law for modes 1444 cm^{-1} and 1610 cm^{-1}, respectively. Considering all concentration, the average RSD for modes at 1444 cm^{-1} and 1610 cm^{-1} are 12.8% and 6.8%, respectively. (For interpretation of the references to colour in this figure legend, the reader is referred to the web version of this article.)

Table 1
Comparison table for detection limit of bilirubin using diverse analytical method.

Materials	Method	Detection limit	References
CoBR complexes	SERS	2×10^{-5} M	He et al. (1995)
ZnBR complexes			
CdBR complexes			
Bilirubin in alkaline aqueous solution	Resonance Raman spectroscopy	2.6×10^{-5} M	Yang et al. (1991)
Diazotized argentiphilic coating.	SERS	1×10^{-6} M	Sulk et al. (1999)
Human serumalbumin stabilized gold nanoclusters	Fluorometric and colorimetric	2.5×10^{-7} M	Santhosh et al. (2014)
Poly-terthiophene–Mn(II) complex/polyethyleneimineascorbate oxidase	Amperometric	4×10^{-8} M	Rahman et al. (2008)
Polyfluorenes with D-glucuronic acid	Fluorescent	1.5×10^{-7} M	Senthilkumar and Asha (2015)
Multilayer enzyme electrode	Cyclicvoltametry	2–4 mg/dl	Shoham et al. (1995)
Au-MoS_2 NFs	SERS	10^{-12} M	This work

SERS signals of both the Raman modes are found to fit the power law dependence of the concentration C^{α} with α 0.12 (for 1444 cm^{-1}) and 0.09 (for 1610 cm^{-1}). From this calibration curve, we can estimate the amount of free bilirubin at an early stage as well as in a fatal condition of liver abnormality quickly and easily. A comparison of detection limit for bilirubin using different analytical methods has been given in Table 1. The table shows that the present SERS method is capable of sensing bilirubin down to 10^{-12} M which has its own significance. Detection and analysis of bilirubin at this low concentration will be advantageous for an early assessment of diseases like diabetic nephropathy, diabetic retinopathy, cardiovascular diseases and chronic kidney diseases.

The reproducibility and stability of the SERS signal of the Au-MoS_2 substrate were examined through the time-dependent measurements on bilirubin with concentration 1×10^{-11} M. The measurements were performed with 1 s integration time and we collected the spectra continuously for 4 min. The integral intensities of the peaks at 1444 and 1610 cm^{-1}, which are obtained by fitting the peaks with Lorentzian functions, are plotted in Fig. S8A. Almost uniform Raman modes are observed throughout the measurement. This result implies that the substrate is highly stable and demonstrates excellent reproducibility.

To show the polarization-dependent SERS response of the substrate we have conducted the measurements at 1×10^{-11} M concentration of bilirubin by varying the polarization of the excitation light. The intensity variation of the mode 1444 and 1610 cm^{-1} with the polarization angle show the quasi-isotropic behavior (see Fig. S8B) which is due to the entangled electromagnetic coupling between several Au NPs on the surface of MoS_2 (Majumdar et al., 2013). Therefore, the nearly polarization independent SERS signal further signifies that the substrate shows high reproducibility.

3.2. Selectivity of the SERS biosensor

To check the reliability of the Au-MoS_2 for biosensing applications, sensing studies of free bilirubin were carried out in HS. A fixed amount of 100 μL of human blood serum was added to 1 mg Au-MoS_2. The analyte, free bilirubin was added directly to Au-MoS_2 and HS mixture with concentration ranging from 1×10^{-3} to 1×10^{-7} M and

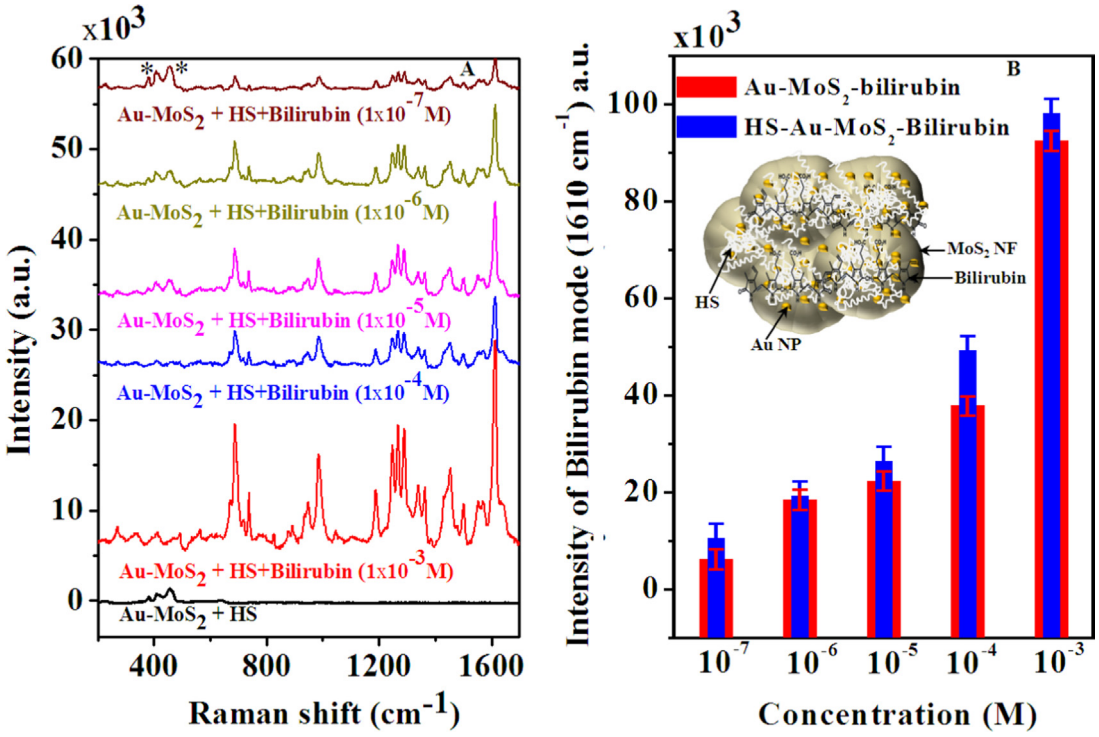

Fig. 5. (A) Concentration (1×10^{-3} M to 1×10^{-7} M) dependent SERS spectra of bilirubin in the presence of HS. Black spectrum is from Au-MoS_2 and HS mixture. Asterisk (*)-marked peaks are from the MoS_2. (B) Bar diagram presents the concentration vs intensity plot of 1610 cm^{-1} mode of bilirubin without HS (red bar) and with HS (blue bar). Inset shows the schematic representation of the adsorption of bilirubin on Au NPs in the presence of HS. Considering all concentration, the average RSD for Au-MoS_2 –Bilirubin and HS-Au-MoS_2–Bilirubin are 7.3% and 10.6%, respectively. (For interpretation of the references to colour in this figure legend, the reader is referred to the web version of this article.)

consequently measured SERS spectra. Fig. 5A clearly shows that Au-MoS_2 is unable to produce any modification in its Raman spectra in presence of HS. Which may be due to the fact that, the HS (containing $\sim 2 \times 10^{-5}$ M total bilirubin which is present mostly in the conjugated form) was not adsorbed on the surface of the Au-MoS_2 hybrid. However, in presence of free bilirubin a spectacular modification in the Raman spectra can be seen (see Fig. 5A) which is due to the strong affinity of bilirubin molecules towards AuNPs (Maity et al., 2014). The intensity of the strongest mode (at 1610 cm^{-1}) is chosen as the marker and compared with the result of Au-MoS_2-bilirubin matrix as depicted in Fig. 5B. The increase in Raman intensity of the 1610 cm^{-1} mode in the presence of HS can be explained if we consider the origin of this Raman band at 1610 cm^{-1}. In the presence of Au-MoS_2 hybrid, the bilirubin molecules undergo deprotonation (both from the -OH and -NH moieties present in bilirubin) due to release of Cl^- ions (Clayden et al., 2012) by the $AuCl_4^-$ species during its transformation to Au(0). The extended conjugation in bilirubin structure leads to molecular rearrangements giving rise to C=N moiety, which give rise to Raman band at 1610 cm^{-1} (Muders et al., 2014). In the presence of HS the –OH and C=O moieties of the bilirubin molecule remain hydrogen bonded with the amino acid parts of the protein present in HS thereby reducing the possibility of deprotonation from -OH group. As a result, the deprotonation now occurs from the NH groups leading to the higher intensity at 1610 cm^{-1} (more of C=N vibrations)

To further validate the feasibility and capability of the SERS platform, Raman assay of bilirubin was also carried out in the presence of elevated concentrations of some interfering species like dextrose, cholesterol and phosphate in HS medium. Although there is a reduction of Raman intensity, it could clearly identify the bilirubin peaks in the presence of such crucial interferences as displayed in Fig. 6. Thus, the study demonstrates the bilirubin sensing ability of Au-MoS_2 NFs with excellent selectivity, reproducibility and high efficiency.

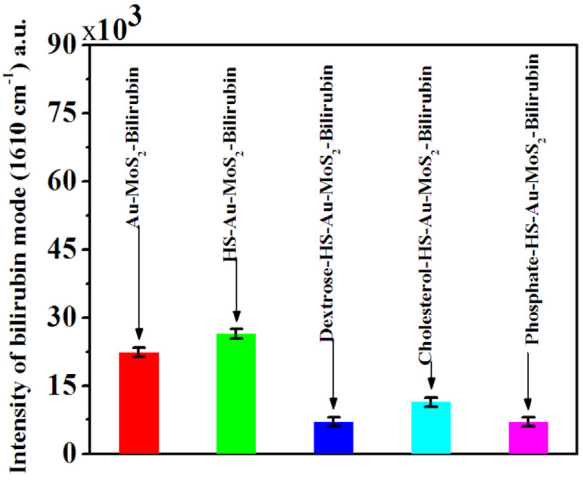

Fig. 6. Bar diagram depicting the Raman intensity of the 1610 cm^{-1} mode of bilirubin when the measurement was performed in Au-MoS_2 + bilirubin (red bar), Au-MoS_2 + HS + bilirubin (green bar), Au-MoS_2 + HS + dextrose + bilirubin (blue bar), Au-MoS_2 + HS + cholesterol + bilirubin (cyan bar), Au-MoS_2 + HS + phosphate + bilirubin (magenta bar). The bilirubin concentration was kept constant at 5×10^{-5} M for all the measurements. The RSD values vary from 4.4% to 14%. (For interpretation of the references to colour in this figure legend, the reader is referred to the web version of this article.)

4. Conclusion

We have successfully synthesized the 3D flower-like MoS_2 nanostructures on a large scale by the hydrothermal method where ~6 nm MoS_2 flakes form the petals. The surface of MoS_2 NFs was uniformly decorated by AuNPs using a simple chemical method. The as-prepared sulphur-rich MoS_2 NF is p-type due to the presence of unbound sulphur

atoms and AuNPs acting as n-type dopants, get stabilized on the MoS_2 surface by strong Au-S interaction. Au NP decoration improves the performance of MoS_2 NFs as SERS substrate. The effect of Au decoration on the electronic and optical property of MoS_2 NF was studied by Raman and PL spectroscopy and the results were explained by charge transfer and Fermi-level realignment phenomena. The sensing ability of the Au-MoS_2 NF was examined through the detection of Rh6G and bilirubin molecules using SERS technique. We have detected free bilirubin from pico-molar level to hyperbilirubinemia state present in human blood. Au NP decoration causes a large enhancement of $\sim 10^9$ for sensing bilirubin molecules compared to bare MoS_2 NF substrate. We have checked the performance of our SERS substrate as a sensor by studying the most important characteristics of a sensor i.e. stability, sensitivity, reproducibility and selectivity. The time-dependent and polarization dependent almost uniform SERS response signifies the high stability and excellent reproducibility of the Au-MoS_2 NF substrate. The selectivity and reliability of this Au-MoS_2 NF platform for biosensing applications have been assured by detecting free bilirubin in human serum in the presence of crucial interferences such as dextrose, cholesterol and phosphate. We thus propose Au-MoS_2 NF substrate as a potential material for sensing toxic biomolecules with high sensitivity and efficiency.

Acknowledgment

The authors are thankful to Mr. Shyam Sundar Mallik of Bose Institute for his help to get XRD data.

Appendix A. Supplementary material

Supplementary data associated with this article can be found in the online version at doi:10.1016/j.bios.2018.07.061.

References

An, Q., Zhang, P., Li, J.-M., Ma, W.-F., Guo, J., Hub, J., Wang, C.-C., 2012. Nanoscale 4, 5210–5216.
Baranano, D.E., Rao, M., Ferris, C.D., Snyder, S.H., 2002. Proc. Natl. Acad. Sci. USA 99, 16093–16098.
Buscema, M., Steele, G.A., van der Zant, H.S.J., Castellanos-Gomez, A., 2014. Nano Res. 7, 561–571.
Chakraborty, B., Bera, A., Muthu, D.V.S., Bhowmick, S., Waghmare, U.V., Sood, A.K., 2012. Phys. Rev. B 85, 161403(R).
Chhowalla, M., Amaratunga, G.A.J., 2000. Nature 407, 164–167.
Cho, S.-Y., Koh, H.-J., Yoo, H.-W., Kim, J.-S., Jung, H.-T., 2017. ACS Sens. 2, 183–189.
Chou, S.S., Kaehr, B., Kim, J., Foley, B.M., De, M., Hopkins, P.E., Huang, J., Brinker, C.J., Dravid, V.P., 2013. Angew. Chem. Int. Ed. 52, 4160–4164.
Clayden, J., Greeves, N., Warren, S., 2012. Organic Chemistry, 2nd ed. Oxford, University Press, UK.
Coleman, J.N., Lotya, M., O'Neill, A., Bergin, S.D., King, P., J., Khan, U., Young, K., Gaucher, A., De, S., Smith, R.J.S., Arora, S.K., Stanton, G., Kim, H.Y., Lee, K., Kim, G.T., Duesberg, G.S., Hallam, T., Boland, J.J., Wang, J.J., Donegan, J.F., Grunlan, J.C., Moriarty, G., Shmeliov, A., Nicholls, R.J., Perkins, J.M., Grieveson, E.M., Theuwissen, K., McComb, D.W., Nellist, P.D., Nicolosi, V., Jonathon, N., 2011. Science 331, 568–571.
Das, A., Pisana, S., Chakraborty, B., Piscanec, S., Saha, S.K., Waghmare, U.V., Novoselov, K.S., Krishnamurthy, H.R., Geim, A.K., Ferrari, A.C., Sood, A.K., 2008. Nat. Nanotechnol. 3, 210–215.
Das, S., Bera, M.K., Tong, S., Narayanan, B., Kamath, G., Mane, A., Paulikas, A.P., Antonio, M.R., Sankaranarayanan, S.K.R.S., Roelofs, A.K., 2016. Sci. Rep. 6, 28195.
Eda, G., Yamaguchi, H., Voiry, D., Fujita, T., Chen, M., Chhowalla, M., 2011. Nano Lett. 11, 5111–5116.
Emory, S.R., Haskins, W.E., Nie, S., 1998. J. Am. Chem. Soc. 120, 8009–8010.
Feldman, Y., Wasserman, E., Srolovitz, D.J., Tenne, R., 1995. Science 267, 222–225.
Fukui, M., Tanaka, M., Shiraish, E., Harusato, I., Hosoda, H., Asano, M., Hasegawa, G., Nakamura, N., 2008. Kidney Int. 74, 1197–1201.
Gan, X., Zhao, H., Quan, X., 2017. Biosens. Bioelectron. 89, 56–71.
Gong, C., Colombo, L., Wallace, R.M., Cho, K., 2014. Nano Lett. 14, 1714–1720.
Graham, D., Thompson, D.G., Smith, W.E., Faulds, K., 2008. Nat. Nanotechnol. 3, 548–551.
He, J., Lu, X.D., Zhou, X., Yu, N.-.T., Chen, Z., 1995. Biospectroscopy 1, 157–162.
Huang, X., Zeng, Z., Bao, S., Wang, M., Qi, X., Fan, Z., Zhang, H., 2013. Nat. Commun. 4, 1444.
Jiang, S., Gup, J., Zhang, C., Li, C., Wang, M., Li, Z., Gao, S., Chen, P., Si, H., Xuc, S., 2017. RSC Adv. 7, 5764–5773.
Junga, G.B., Baeb, Y.M., Leea, Y.J., Ryud, S.H., Park, H.-K., 2013. Appl. Surf. Sci. 282, 161–164.
Kong, D., Wang, H., Cha, J.J., Pasta, M., Koski, K.J., Yao, J., Cui, Y., 2013. Nano Lett. 13, 1341–1347.
Krishnamoorthy, K., Veerasubramani, G.K., Radhakrishnan, S., Jae, S., 2014. Mater. Res. Bull. 50, 499–502.
Kushim, A., Qian, X., Zhao, P., Zhang, S., Li, J., 2015. Nano Lett. 15, 1302–1308.
Lauritsen, J.V., Kibsgaard, J., Helveg, S., Topsoe, H., Clausen, B.S., Legsgaard, E., Besenbacher, F., 2007. Nat. Nanotechnol. 2, 53–58.
Lee, C., Yan, H., Brus, L.E., Heinz, T.F., Hone, J., Ryu, S., 2010. ACS Nano 4, 2695–2700.
Lee, K., Gatensby, R., McEvoy, N., Hallam, T., Duesberg, G.S., 2013. Adv. Mater. 25, 6699–6702.
Lee, K., Drachev, V.P., Irudayaraj, J., 2011. ACS Nano 5, 2109–2117.
Liang, X., Zhang, X.J., You, T.T., Yang, N., Wang, G.S., Yin, P.G., 2018. J. Raman Spectrosc. 49, 245–255.
Li, H., Chen, Q., Hassan, Md. M., Chen, X., Ouyang, Q., Guo, Z., Zhao, J., 2017. Biosens. Bioelectron. 92, 192–199.
Lin, E.C., Fang, J., Park, S.C., Stauden, T., Pezoldt, J., Jacobs, H.O., 2013. Adv. Mater. 25, 3554–3559.
Ling, X., Fang, W., Lee, Y.-H., Araujo, P.T., Zhang, X., Rodriguez-Nieva, J.F., Lin, Y., Zhang, J., Kong, J., Dresselhaus, M.S., 2014. Nano Lett. 14, 3033–3040.
Lu, J., Lu, J.H., Liu, H., Liu, B., Gong, L., Tok, E.S., Loh, K.P., Sow, C.H., 2015. Small 11, 1792–1800.
Ma, L., Chen, W.-X., Li, H., Zheng, Y.-F., Xu, Z.-D., 2008. Mater. Lett. 62, 797–799.
Maity, M., Das, S., Maiti, N.C., 2014. Phys. Chem. Chem. Phys. 16, 20013–20022.
Majumdar, D., Singha, A., Mondal, P.K., Kundu, S., 2013. ACS Appl. Mater. Interfaces 5, 7798–7807.
McDonnell, S., Addou, R., Buie, C., Wallace, R.M., Hinkle, C.L., 2014. ACS Nano 8, 2880–2888.
Mdleleni, M.M., Hyeon, T., Suslick, K.S., 1998. J. Am. Chem. Soc. 120, 6189–6190.
Mouri, S., Miyauchi, Y., Matsuda, K., 2013. Nano Lett. 13, 5944–5948.
Muders, V., Kerruth, S., Fonfría, V.A.L., Bamann, C., Heberle, J., Schlesinger, R., 2014. FEBS Lett. 588, 2301–2306.
Polyakov, Y.A., Yadgarov, L., Popovitz-Biro, R., Lebedev, V.A., Pinkas, I., Rosentsveig, R., Feldman, Y., Goldt, A.E., Goodilin, E.A., Tenne, R., 2014. J. Phys. Chem. C 118, 2161–2169.
Qian, X.-M., Nie, S.M., 2008. Chem. Soc. Rev. 37, 912–920.
Radisavljevic, B., Radenovic, A., Brivio, J., Giacometti, V., Kis, A., 2011. Nat. Nanotechnol. 6, 147–150.
Rahman, Md. A., Lee, K.-S., Park, D.-S., Won, M.-S., Shim, Y.-B., 2008. Biosens. Bioelectron. 23, 857–864.
Ramadoss, A., Kim, T., Kim, G.-S., Kim, S.J., 2014. New J. Chem. 38, 2379–2385.
Rao, C.N.R., Govindaraj, A., 2009. Adv. Mater. 21, 4208–4233.
Santhosh, M., Chinnadayyala, S.R., Kakoti, A., Goswami, P., 2014. Biosens. Bioelectron. 59, 370–376.
Sekioka, R., Tanaka, M., Nishimura, T., Itoh, H., 2015. Diabetol. Int. 6, 300–305.
Senthilkumar, T., Asha, S.K., 2013. Macromolecules 46, 2159–2171.
Senthilkumar, T., Asha, S.K., 2015. Macromolecules 48, 3449–3461.
Shi, Y., Huang, J.-K., Jin, L., Hsu, Y.-T., Yu, S.F., Li, L.-J., Yang, H.Y., 2013. Sci. Rep. 3, 1839.
Shoham, B., Migron, Y., Riklin, A., Willner, I., Tartakovsky, B., 1995. Biosens. Bioelectron. 10, 341–352.
Singha, S.S., Nandi, D., Singha, A., 2015. RSC Adv. 5, 24188–24193.
Singha, S.S., Nandi, D., Bhattacharya, T.S., Mondal, P.K., Sinhga, A., 2017. J. Alloy. Compd. 723, 722–728.
Splendiani, A., Sun, L., Zhang, Y., Li, T., Kim, J., Chim, C.-Y., Galli, G., Wang, F., 2010. Nano Lett. 10, 1271–1275.
Sreeprasad, T.S., Nguyen, P., Kim, N., Berry, V., 2013. Nano Lett. 13, 4434–4441.
Su, S., Zhang, C., Yuwen, L., Chao, J., Zuo, X., Liu, X., Song, C., Fan, C., 2014. ACS Appl. Mater. Interfaces 6, 18735–18741.
Sulk, R., Chan, C., Guicheteau, J., Gomez, C., Heyns, J.B.B., Corcoran, R., Carron, K., 1999. J. Raman Spectrosc. 30, 853–859.
Tanaka, M., Fukui, M., Okada, H., Senmaru, T., Asano, M., Akabame, S., Yamazaki, M., Tomiyasu, K.-I., Oda, Y., Hasegawa, G., Toda, H., Nakamura, N., 2014. Atherosclerosis 234, 421–425.
Tang, G., Wang, Y., Chen, W., Tang, H., Li, C., 2013. Mater. Lett. 100, 15–18.
Tenne, R., 2006. Nat. Nanotech. 1, 103–111.
Veeramalai, C.P., Li, F., Xu, H., Kim, T.W., Guo, T., 2015. RSC Adv. 5, 57666–576670.
Vollath, D., Szabó, D.V., 1998. Mater. Lett. 35, 236–244.
Wang, D., Pan, Z., Wu, Z., Wang, Z., Liu, Z., 2014. J. Power Sources 264, 229–234.
Wang, W., Li, L., Wu, K., Zhu, G., Tan, S., Li, W., Yang, Y., 2015. RSC Adv. 5, 61799–61807.
Wei, X., Su, S., Guo, Y., Jiang, X., Zhong, Y., Su, Y., Fan, C., Lee, S.-T., He, Y., 2013. Small 9, 2493–2499.
Wu, Z., Li, B., Xue, Y., Li, J., Zhang, Y., Gao, F., 2015. J. Mater. Chem. A 3, 19445–19454.
Xie, J., Zhang, H., Li, S., Wang, R., Sun, X., Zhou, M., Zhou, J.F., Lou, X.W. (David), Xie, Y., 2013. Adv. Mater. 25, 5807–5813.
Xu, L.-M., Zhou, X.-P., Xu, X.-Y., 2014. Mater. Lett. 132, 291–294.
Yan, Y., Xia, B.Y., Ge, X., Liu, Z., Wang, J.-Y., Wang, X., 2013. ACS Appl. Mater. Interfaces 5, 12794–12798.
Yang, B.J.D., Morris, Michael, Xie, M., David, A., 1991. Biochemistry 30, 694.
Yigit, M.V., Zhu, L., Ifediba, M.A., Zhang, Y., Carr, K., Moore, A., Medarova, Z., 2011. ACS Nano 5, 1056–1066.
Yuwen, L., Xu, F., Xue, B., Luo, Z., Zhang, Q., Bao, B., Su, S., Weng, L., Huang, W., Wang, L., 2014. Nanoscale 6, 5762–5769.
Zelenski, M.C., Dorhout, P.K., 1998. J. Am. Chem. Soc. 120, 734–742.
Zeng, Z., Yin, Z., Huang, X., Li, H., He, Q., Lu, G., Boey, F., Zhang, H., 2011. Angew. Chem. Int. Ed. 50, 11093–11097S.